LAWRENCE
LIVERMORE
NATIONAL
LABORATORY

LLNL-JRNL-825755

Fourier method for 3-Dimensional Data Fusion of X-ray Computed Tomography and Ultrasound

W. K. Leach, J. Lum, S. Azevedo, K. Champley, C. Gardner, H. Kim, D. Stobbe, A. Townsend

August 13, 2021

Non-destructive Testing and Evaluation International

Disclaimer

Fourier method for 3-Dimensional Data Fusion of X-ray Computed Tomography and Ultrasound

William Leach[a,*], Jordan Lum[a], Kyle Champley[a], Stephen Azevedo[a], Casey Gardner[a], Hyojin Kim[a], David Stobbe[a], Andrew Townsend[a], Joe Tringe[a]

[a] *Lawrence Livermore National Laboratory, 7000 East Ave, Livermore, CA 94551, USA*

* Corresponding Author. Email address: champley1@llnl.gov (K. Champley)

Abstract

X-ray Computed Tomography (CT) is essential for nondestructive inspection of many manufactured components but is susceptible to various forms of artifacts and noise. In particular, multi-detector row cone-beam CT systems can suffer from so called "cone-beam" artifacts and partial volume effects, particularly on planar edges at the periphery of the field of view in the cone angle dimension. Uni-directional ultrasonic testing methods generally have extremely accurate in-plane depth resolution but poorer lateral resolution due to physical and geometric constraints. This paper presents a novel technique called Computed Tomographic Fusion (CT-F) which uses three-dimensional Fourier filtering to combine x-ray cone-beam CT reconstructions and ultrasound data in the frequency space. The result is a single image with improved accuracy and quality. CT-F mitigates artifacts while allowing for rapid, accurate characterization of large three-dimensional CT volumes. Using simulations and experiments, we demonstrate artifact reduction and edge contrast improvement in volumetric reconstructions.

Keywords: X-ray Tomography, Ultrasound, Multi-modal Data Fusion, Cone-beam Artifacts

1. Introduction

X-ray and acoustic measurements can be complementary for understanding structural and mechanical properties of complex objects. Cone-beam x-ray CT is an established technique for characterizing objects in three dimensions. However, the CT reconstruction process, which enables 3D volumetric measurements of internal structures and surfaces as well as local attenuation, is subject to artifacts which are often difficult to identify and resolve. These artifacts come in the form of streaks and loss of object boundaries that challenge quantitative measurement and can reduce contrast. Ultrasound measurements, which are sensitive to density discontinuities, can be used to resolve some of these ambiguities. Each technique can inform the other if data is spatially registered and combined systematically. Some research has been done for human health applications to align ultrasound, x-ray CT and other modalities in real-time [1,2]. However, these methods either display the modalities side by side or simply superimpose them, which does not provide a direct quantitative improvement in accuracy. Other work in non-destructive testing (NDT) has shown systematic integration using two-dimensional slices or exterior object surfaces [3,4], but those accuracy improvements are also limited due to the non-volumetric nature of the methods.

In section 2 of this paper, we present background and the theory of the artifacts common to cone-beam CT. In section 3 we demonstrate volume registration and data fusion using simulated data. In section 4 we present test object design, data acquisition methods, as well as

measured data. In section 5 we demonstrate registration and fusion results using the measured data.

2. Cone-beam CT Background

Circular source trajectory cone-beam CT systems can rapidly provide a 3D scan with one rotation. These systems are frequently used due to their straightforward implementation compared to alternative (e.g., helical, saddle) trajectories. However, it is known [5,6,7] that circular trajectories fail to collect all the data necessary for a complete reconstruction if the object of interest has components that lie outside of the plane containing the source trajectory (also known as the source plane). The geometrical limitations of these trajectories may distort or misrepresent features not in the source plane and can lead to missing data in CT reconstructions.

There are many interpretations [5,8] of the missing data in circular trajectory cone-beam reconstructions, but our method is motivated by the fact that the missing information relates to a shift-variant cone of corrupted spatial frequency components in the Fourier transform of the reconstruction [9]. For a given point in the object that is above or below the source plane, there is a set of missing plane integrals that correspond to a conical region of missing spatial frequency components in the Fourier domain. Each point's missing component region has a unique cone shape and angle, but the boundaries of the cone are defined by the half cone angle of the x-ray CT system. The theoretical issues behind this are explored in the next section.

2.1 Cone-beam CT Theory

The measured axial cone-beam projections g may be modeled by the line integral transform of the density function $f: \mathbb{R}^3 \rightarrow \mathbb{R}$ of the object along the path from source to detector

$$g(\varphi, \Theta) = \int_{\mathbb{R}} f(R\theta(\varphi) + l\Theta)dl,$$

where R is the distance from the source to the center of rotation, φ is the parameter describing the source position $\theta(\varphi)$, $\theta(\varphi) = (\cos\ \varphi, \sin\ \varphi, 0)^T$, and Θ is the source to detector trajectory of the x-rays. We define the inverse three dimensional Fourier transform by

$$f(x) = \int_{\mathbb{R}^3} \hat{f}(\xi) e^{2\pi i <x,\xi>} d\xi.$$

Then the axial cone-beam data may be represented by

$$\begin{aligned} g(\varphi, \Theta) &= \int_{\mathbb{R}} \int_{\mathbb{R}^3} \hat{f}(\xi) e^{2\pi i <R\theta(\varphi)+l\Theta,\xi>} d\xi dl \\ &= \int_{\mathbb{R}^3} \hat{f}(\xi)\delta(\xi \cdot \Theta) e^{2\pi i <R\theta(\varphi),\xi>} d\xi \end{aligned} \quad (1)$$

Eq. (1) implies that the projection data given by $g(\varphi, \Theta)$ is related to the frequencies of $\hat{f}(\xi)$, where $\xi \cdot \Theta = 0$. Now consider all the projections through a point $\boldsymbol{x} \in \mathbb{R}^3$. These projections are given by $\Theta = \frac{\boldsymbol{x} - R\theta(\varphi)}{\|\boldsymbol{x} - R\theta(\varphi)\|}$. Thus, the projections contribute to the frequencies of $\hat{f}(\xi)$ at the spatial location $\boldsymbol{x}$ given by the 2D plane

$$\xi \cdot (\boldsymbol{x} - R\theta(\varphi)) = 0,$$

or equivalently,

$$\xi_1(R\cos\ \varphi - x_1) + \xi_2(R\sin\ \varphi - x_2) = \xi_3 x_3. \quad (2)$$

We define the set of frequencies given by Eq. (2) for all $\varphi \in [0, 2\pi)$ by

$$\omega(x) := \{\xi \in \mathbb{R}^3 : \xi_1(R\cos\ \varphi - x_1) + \xi_2(R\sin\ \varphi - x_2) = \xi_3 x_3, \varphi \in [0, 2\pi)\} \quad (3)$$

This set consists of all the frequencies in $\mathbb{R}^3$ except those inside an elliptical cone with an axis along the ξ_3 axis. Note that when x is in the plane given by $x_3 = 0$, $\omega(x) = \mathbb{R}^3$ and when $x_3 \neq 0$ then $\omega(x) \subsetneq \mathbb{R}^3$, where the missing frequencies lie within the previously mentioned elliptical cone. The aperture of this cone is dictated by the co-polar angle of the line from the source to the point, x, in the imaging volume. Sketches of these two cases are shown in Fig. 1.

This missing cone of frequencies is the theoretical explanation for so-called cone-beam artifacts, and it is the result of certain frequencies of the reconstructed volume f that are not determined by the x-ray projection data. These artifacts manifest themselves as loss of resolved edges (edges are blurred) whose gradients are essentially parallel to the z-axis.

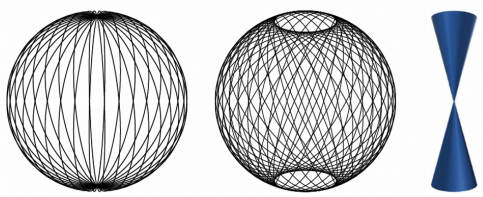

Fig. 1. Sketches of the recoverable frequencies of $\hat{f}$ for (a) points that lie in the source plan $x_3 = 0$ and (b) points that do not lie in the source plane $x_3 \neq 0$ The missing frequencies for the center sketch are shown in (c).

3. Correcting Cone-beam Artifacts

Correcting these cone-beam artifacts, therefore, requires that the missing Fourier data be modeled, measured, or estimated. Some examples of these methods are region-of-interest in the Radon space [10], multiple scan correction techniques [11], and regularized iterative methods [12,13]. In our case, we studied how ultrasound could be used on the axially oriented surfaces of

homogeneous objects and integrated with x-ray CT in the Fourier domain to improve 3D reconstructions.

3.1 Ultrasound Interrogation

Assuming knowledge of the acoustic properties of the object and access to its surface, scanning immersion ultrasound data (3D C-scan) can be used to resolve some of the missing CT data. The general process for acquiring the C-scan data used in this paper is described below. A more comprehensive description of immersion ultrasound systems and measurement is provided at the corresponding material [14,15].

Here, our goal is to create a 3D volume of the component under study using immersion ultrasound C-scan measurements. This is done by scanning the top and bottom of the sample and collecting a 1D A-scan at each x, y position (see Fig. 10 for more detail). Each A-scan is processed assuming the object is homogeneous and then the first measured echo is used to determine the distance from the scanning surface to the next nearest surface within the part. Then the measured C-scan images, from the top and bottom of the sample, can be resampled in the x, y dimensions to match the x-ray CT voxel resolution. To enable registration and data fusion with the CT reconstructed volume, the material thickness values at each x, y position are converted into volumes, with voxels assigned a value of the mean x-ray CT Linear Attenuation Coefficient in the material and zero for air/void.

3.2 Registration of X-ray and Ultrasound Volumes

Proper alignment of the CT reconstruction volume v and ultrasound volume m is a necessary step prior to fusion. Assuming the volumes have been properly scaled to the same resolution then three-dimensional rigid (translation and rotation) registration is required. This is performed by a standard gradient descent optimization using the mean squared distance between the volumes' intensities as the similarity metric (Eq. 4). This technique is commonly used in medical image registration [16,17]. The algorithm works by iteratively updating the six translational and rotational transformation parameters Φ along the negative of their gradient with respect to the distance metric d until the metric is minimized. d is calculated for each voxel p over Ω, where $\Omega \subset \mathbb{R}^3$ are the coordinates of the reconstruction region and T is the affine transformation matrix for Φ.

$$d(\Phi) = \sum_{p \in \Omega} \left[m(p) - v\left(T(p; \Phi)\right) \right]^2 \qquad (4)$$

3.3 Fourier-space Data Fusion

The CT-F algorithm consists of a three-dimensional weighting in the Fourier domain, with a cone shaped filter H shown in Fig. 2. This filter was designed this way for two reasons: the cone shape agrees with the largest cone of missing frequencies from the cone-beam CT acquisition. In addition, this filter also takes advantage of the fact that immersion ultrasound has better resolution than cone-beam CT in the axial (z) direction and poorer resolution in the lateral (x, y) direction. We specified the filter, H, by

$$H(X,Y,Z) = h_{Gaussian} * \begin{Bmatrix} 1, & (z\tan\beta)^2 > X^2 + Y^2 \\ 0, & otherwise \end{Bmatrix}$$

where the Gaussian function is designed to smooth the boundaries of the function to enable to smooth blending of the two volumes. We used a Gaussian function with a three-pixel full width at half maximum. Typically, the angle β is chosen as the maximum cone angle of the x-ray CT system but could be considered a tuning parameter. This filter incorporates more of the UT volume than is necessary to correct for cone-beam artifacts in slices near the midplane. We chose to do this to make the filtering process stationary invariant so that we can employ FFT operations and to take more advantage of the excellent depth resolution of the UT volume.

The filter h is applied to the ultrasound volume m, and the inverse of this filter $(1-h)$ is applied to the x-ray CT volume v. This is done by transforming the ultrasound and x-ray CT volumes to their Fourier domains M, V, and by multiplying the resulting frequency component volumes by their respective filters $H, (1-H)$, respectively. Then the inverse Fourier transform of the sum of the two frequency component volumes is taken as the final fused result f:

$$f = m * h + v * (1-h) = F^{-1}[F(w)] = F^{-1}\big(MH + V(1-H)\big) \quad (5)$$

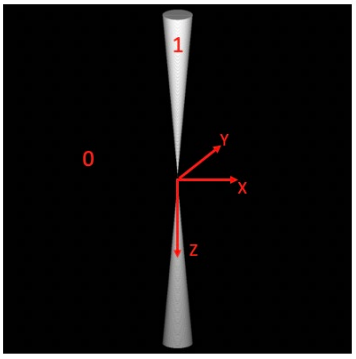

Fig. 2. Frequency response H(X,Y,Z) of filter h used on ultrasound volume. H has the value one in the two conical regions and zero elsewhere. The inverse filter (1-H), where the one and zero regions are reversed, was applied to the x-ray CT reconstruction.

3.4 CT-F using Simulated Data

Next, we show that CT-F can improve the imaging of a simulated homogeneous cylindrical object with internal voids, as shown in Fig. 3. We modeled this object and simulated the results of x-ray and ultrasound inspections. The object contains a series of four concentric circular air-filled grooves of different diameters and depths.

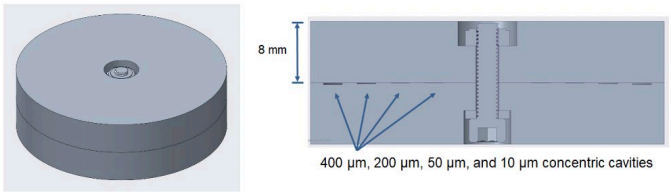

(a) (b)

Fig. 3 Rendering (a) and central vertical slice (b) of a simulated homogeneous test object containing concentric circular grooves. The outside diameter is 89 mm (3.5 inches).

A simulated ultrasound reconstruction of this object (in Fig. 4) was generated by creating a binary voxel map (one for material and zero for air/void) using the expected spatial resolution estimates for the experimental scans that will be described in section 4.4. The horizontal slice (x, y) appears pixelated because the ultrasound A-scan samples in x and y are sparse whereas the z sampling is fine.

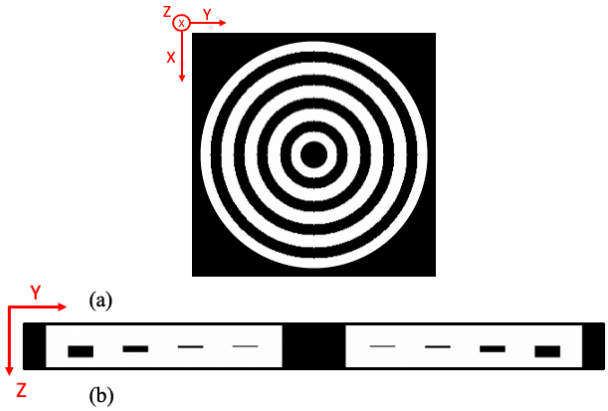

Fig. 4. Ultrasound simulated images of (a) the central horizontal slice and (b) the central vertical slice of the test object. Note that since this object is circularly symmetric, all central vertical planes should be identical.

Cone-beam x-ray projections of this object were simulated with 720 projections over 360 degrees. The central fan was aligned with its bottom edge. Detector parameters were modeled to roughly match our experimental CT system (2048 x 2048 square pixels each with side length 0.2 mm) and the projected x-rays were simulated at 63 keV (monochromatic).

Both the x-ray simulations and 3D reconstructions were performed with the Livermore Tomography Tools (LTT) software package [18]. All cone-beam reconstructions in this paper were performed using the Feldkamp-David-Kress (FDK) algorithm [19]. For the above test object, the reconstruction voxel size was 0.04 mm x 0.04 mm x 0.02 mm (0.02 mm in z-coordinate).

The central vertical (y, z) and horizontal (x, y) 2D slice images of the FDK cone-beam reconstruction are shown in Fig. 5. In this case, the inner two grooves are distorted and exhibit

lower contrast. These effects are caused by both the cone-beam artifacts and the partial-volume effect.

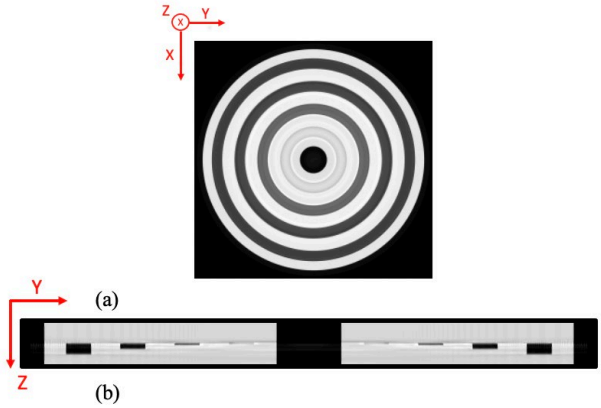

Fig. 5. Cone-beam reconstructed images of (a) the central horizontal slice and (b) the central vertical slice of the test object. Cone-beam and partial-volume effects reduce visibility of the smallest grooves.

Using the CT-F algorithm as described in the previous section, all grooves become more distinct and visible as shown in Fig. 6. The aperture of the cone-shaped filter, β, was chosen to be five degrees.

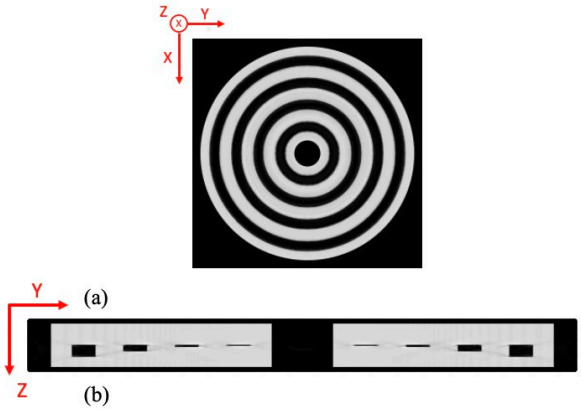

Fig. 6. Fused cone-beam x-ray and ultrasound reconstructed images of (a) the central horizontal slice and (b) the central vertical slice of the test object. CT artifacts are reduced compared to cone-beam alone.

This test object, although it was simulated with no additional noise or registration issues, shows that much of the cone-beam and partial-volume effects can be suppressed by augmenting missing sections of the Fourier domain with ultrasound information. Next, CT-F is implemented on experimentally measured data.

4. Experiments

To demonstrate the application of our fusion method with measured data, we designed a test object with multiple internal voids of known dimensions. We then performed cone-beam CT and ultrasound C-scans to evaluate the CT-F algorithm.

4.1 Test Object

The test object consists of two 88.9 mm diameter, 8 mm thick Rexolite® disks assembled with a central polypropylene bolt and nut (Fig. 7(a)). Rexolite® is a translucent, rigid thermoset plastic produced by cross linking polystyrene with divinylbenzene. One disk contains five concentric grooves machined into one of the faces (Fig. 7(b)); these grooves are in the same thickness ranges as the four grooves in the simulated object.

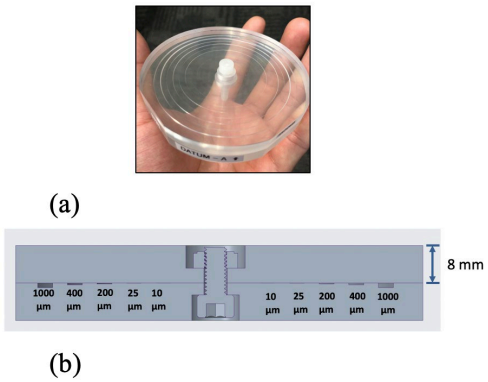

Fig. 7. Test object; mounting bolt and concentric grooves visible (a), CAD model side view of test object with groove dimensions (b).

4.2 Cone-beam X-ray CT Measurements

X-ray CT measurements were performed using a cone-beam configuration with a Yxlon Microfocus source (FXE-225.48-3) and 4096 x 4096 pixel 16 bit flat panel PerkinElmer detector (XRD-1611-AP26) with pixel size of 100 µm. The source voltage was 200 kV at a current of 200 mA with an integration time of 6 seconds. The source to detector and source to object distances were 308.5 mm and 1204.5 mm, respectively. As in the simulation, the central fan was aligned with its bottom edge. A 4 mm Copper filter was used, and 1440 projections were acquired with an angular range of 360°. The projections were reconstructed to a voxel size of 50 µm and cropped to 1850 x 1850 x 400 voxels in the x, y, z dimensions.

The CT reconstruction, together with a lineout along the axial dimension (z), is shown in Fig. 8. Cone beam blurring is visible along the top edge of the object in the central vertical slice (Fig. 8(c)). In addition the two inner most grooves are not discernable in the raw x-ray CT scan

due to their small heights (25 and 10 µm). The goal with fusion is to supplement this missing information with the axially oriented edge data in the ultrasound volume.

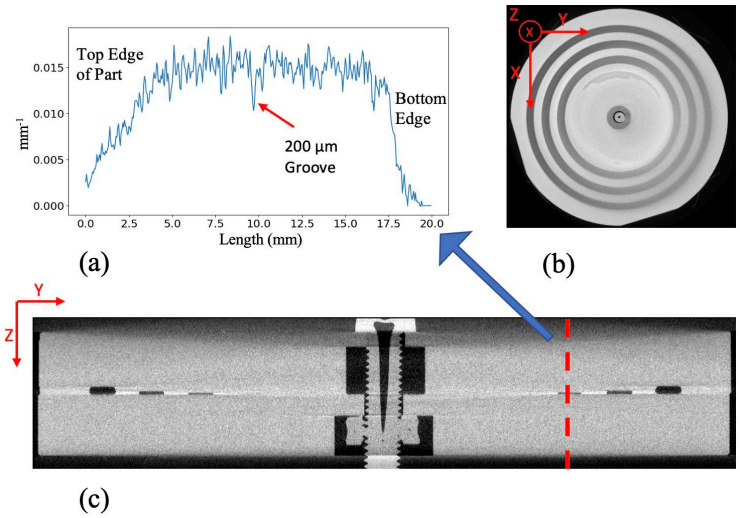

Fig. 8. X-ray CT reconstruction central vertical slice lineout (a) with central horizontal slice (b) and central vertical slice (c). The lineout shows that the bottom edge is much more defined (because the x-ray source is aimed at this edge during measurement).

4.3 Immersion Ultrasound Measurements

A three-axis motion control immersion tank system (Mistras Group, Inc.) was used to conduct immersion ultrasound C-scan imaging of each half of the Rexolite part (Fig. 9). The object was scanned in a pulse-echo mode with a 6.35 mm diameter, single element, spherically focused immersion transducer (Panametrics, V313) with 15 MHz center frequency. The longitudinal wave speed of Rexolite material was measured to be 2333 m s^{-1}. The transducer was positioned so its focal point was at the midplane of the object and was raster scanned across the surface in 63.5 µm steps in the x and y directions, which was the minimum step size for this

system. After scanning one side, the sample was rotated and raster scanned again. Although the two halves of the sample were mechanically pressed together with a set screw, the ultrasonic waves did not couple past the midplane interface. This interface was used as the back wall when scanning both sides. The A-scans at each x, y position had a sampling frequency of 250 MHz and were recorded after 20 signal averages to improve the signal-to-noise ratio.

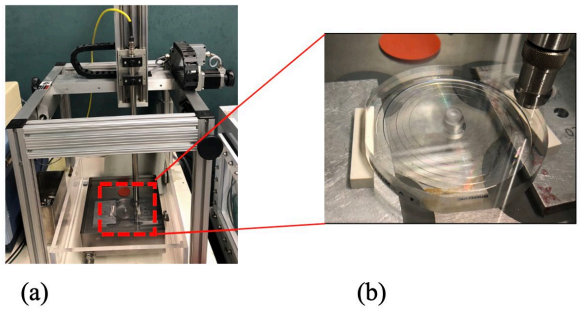

Fig. 9. Experimental setup for immersion ultrasound measurements (a). Zoomed in image showing sample and immersion sensor (b).

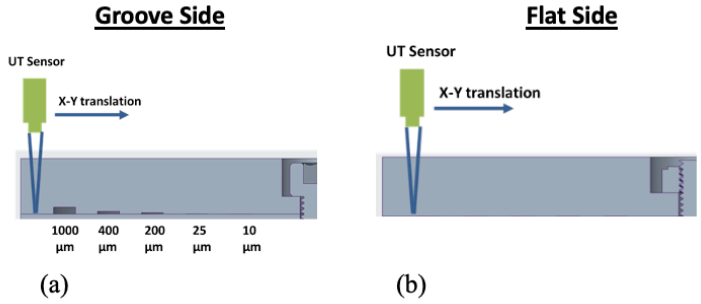

Fig. 10. Illustration of immersion ultrasound scanning procedure taking scans from top (a) and bottom (b) of sample.

4.4 Generating a Volume from Immersion Ultrasound Measurements

To apply the CT-F technique, the ultrasound measured data were converted into a three-dimensional volume format. Using the ultrasound interrogation technique described in section 3.1, C-scan images were acquired for the top and bottom sides of the object by calculating the one-sided thickness of the part using each measured A-scan. The images were then resampled in the x, y dimensions from 63.5 μm spacings to 50-μm spacings using a linear interpolation function. Thickness values at each new x, y position were converted into volumes, with voxels assigned a value of the x-ray Linear Attenuation Coefficient to indicate Rexolite material and voxels assigned a value of zero to indicate no Rexolite material. This scaling makes the UT volume resemble the scaling of the x-ray CT volume. Additional zero-valued voxels were added to surround the volume, resulting in a final volume size of 1850 by 1850 by 400 voxels in the x, y, z dimensions.

The measured ultrasound volume is shown in Fig. 11. The central horizontal slice (Fig. 11(a) appears pixelated because the ultrasound resolution in the x, y dimensions is limited by the spot size of the sensor and beam diffraction at the edges. However, along the axial dimension (z direction) the ultrasound data is precise due to the temporal resolution and planar surfaces. The center of the volume was removed since this was the area where the set screw was used to hold the sample together.

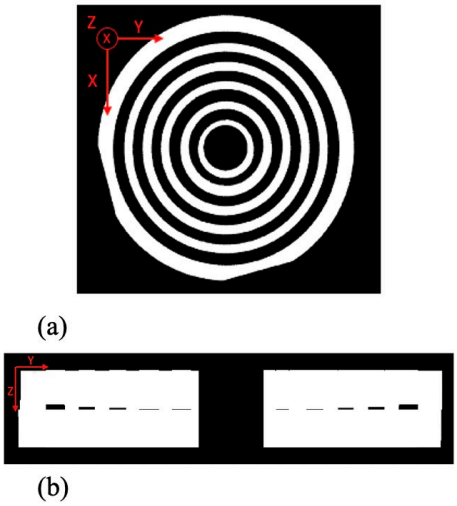

Fig. 11. Ultrasound data in volume format central horizontal slice (a) and central vertical slice (b). Depth resolution (z direction) is higher than lateral resolution (x, y) due to spot size and discrete lateral positioning of ultrasound sensor during measurement.

5. Results

Fusion of the CT and ultrasound data required the following steps: registering the two 3D volumes in space, transforming them to the Fourier domain, combining them as in Eq. (5), then performing an inverse Fourier transform to achieve the final volume.

5.1 Registration

The complementary nature of the two modalities is motivation for data fusion, providing they are adequately registered. Different forms of information representation in each modality, however, makes intensity-based registration optimization challenging. The process for automated data registration used in this study is described next.

To begin, the x-ray CT and ultrasound volumes were manually pre-aligned to roughly the same orientation. Next, the histogram of the intensities in the x-ray CT volume was calculated. The assumption was made that the histogram would have a bimodal characteristic due to the homogeneity of the material in the sample. A Gaussian distribution was fit to the second peak in the histogram corresponding to the regions containing material within the x-ray CT reconstruction. The estimate of the average value of the sample was calculated by taking the mean of the fitted Gaussian. Then all non-zero voxels of the ultrasound volume $v \in \Omega_s$ (where Ω_s are the voxel coordinates of the ultrasound volume with material) were set to the mean μ of the Gaussian (.015 mm^{-1}) as shown in Eq. 6. This resulted in an improved match between the intensity distributions of the two volumes.

$$v_i = \begin{cases} \mu \; if \; i \in \Omega_s \\ 0 \text{ if i } \notin \Omega_s \end{cases} \tag{6}$$

For registration itself a multi-scale data reduction approach was applied. First the ultrasound volume is scaled to the resolution of the x-ray CT volume following the process describe in section 4.4. Then the resolution of the volumes was sequentially decreased by a factor of two, 3 times, and the gradient-based optimization (Eq. 4) began with the coarsest resolution level. The output from the resulting transformation was used to initialize the next optimization at the next resolution level. The process was continued 3 times until the original, full resolution was reached. The same optimization was run once more on the volumes at full resolution but with a significant reduction in the gradient tolerance and minimum gradient step

size relative to the values used in the multi-scale stages. The registrations were performed with the image processing toolbox from MATLAB [20].

The hyperparameters used for optimization for both stages are shown in Table 1; these values were found empirically to result in the best registration. The results are shown in Fig. 12 where it is seen that the volumes, particularly the edges in the axial z dimension, are well aligned after registration. Slight mismatches can be seen along the lateral y dimension (which are due to the step size limits of the ultrasound scanner rather than registration limitations). The improvement in the Pearson correlation coefficient and mutual information, respectively, of the two volumes after registration are shown in Table 2. The filtering methods and fusion of the x-ray CT and ultrasound data are described in the next section.

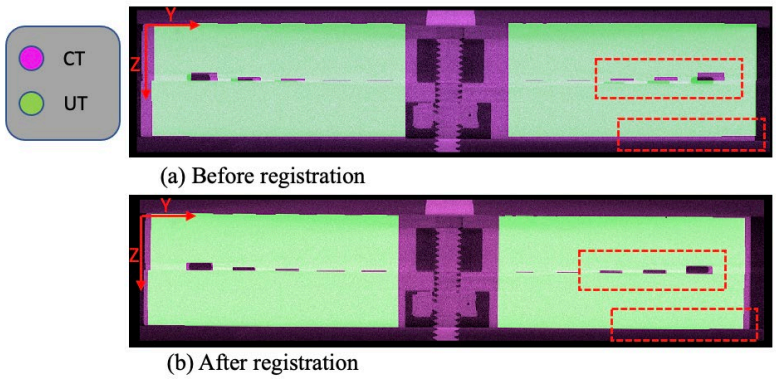

Fig. 12. Central vertical slice of x-ray CT and ultrasound alignment before (a) and after (b) registration. Edges in the z-direction are well aligned after registration, highlighted by the red boxes.

Table 1. Gradient Optimization parameters for registration.

Optimizer Parameters	Multi-scale Values	Full Resolution Values
Resolution Levels	3	1 (run on full resolution)

Iterations per level	300	300
Gradient Tolerance	$1.0x10^{-06}$	$1.0x10^{-07}$
Minimum Gradient Step Size	$5.0x10^{-07}$	$1.0x10^{-07}$

Table 2. Metrics before and after registration.

Metric	Before Registration	After Registration
Correlation Coefficient	.833	.876
Mutual Information (normalized)	.083	.086

5.2 Fusion Results

The performance of this fusion method was demonstrated by applying our model (Eq. 5) to the test object described in section 4.1. Volume sizes were 1850 x 1850 x 400 voxels in the x, y, z dimensions, highlighting the capability of the algorithm to efficiently process large, three-dimensional reconstructions. The aperture of the cone-shaped filter, β, was chosen to be five degrees. In addition, the fusion algorithm runs in under 6 minutes on a workstation with 2 Xeon® E5-2695 processors.

Commented [CKM1]: William, how did you perform the filtering? Did you do this in MATLAB? This seems very slow.

Improvement of the fused approach over x-ray CT alone is illustrated by the CT reconstructions and fused results seen in Fig. 13 and Fig. 14. The central horizontal slice and its lineout along the y direction in Fig. 13(b) show an increase in the contrast and intensity consistency between each of the grooves. In addition, the previously undiscernible innermost grooves are now visible. From the central vertical slices, as seen in Fig. 14(b), the smearing artifacts along axial edges in the cone beam dimension (z axis) are also reduced. The top edges

of the sample and the grooves (200 µm groove shown in detail in Fig. 14) are now clearly defined.

To offer a simple quantitative evaluation of the fusion method, both an image quality and quantitative metric were calculated. The contrast-to-noise ratio (CNR) of two regions C1, C2 (Fig. 14) in the cross-sectional side view images was used to quantify image quality:

$$CNR = \frac{|\mu_m - \mu_b|}{\sigma_b} \quad (7)$$

where μ_m is the mean of a region containing material, and μ_b, σ_b are the mean and standard deviation of the background, respectively.

The regions C1 and C2 are taken on the boundary at the edge of the sample, and at the 200 µm groove to focus on the areas where fusion improvement would be highlighted. The results are shown for x-ray CT in Table 3 and support the qualitative improvement in contrast in edges at both the boundary and inner voids of the sample that are seen in the image results. The CNR is not listed for ultrasound due to the binary nature of the data.

In a second method, the enhancement in measurement capabilities was tested by estimating the height of the sample and the 200 µm groove and comparing the results to specifications. The widths were calculated by taking the full-width half-maximum (FWHM) of the peaks defined by the edges in the lineout drawn from the cross-sectional images as shown in Fig. 14. The estimates are listed in Table 4 showing improvement in the metrological capabilities of fusion over either modality alone.

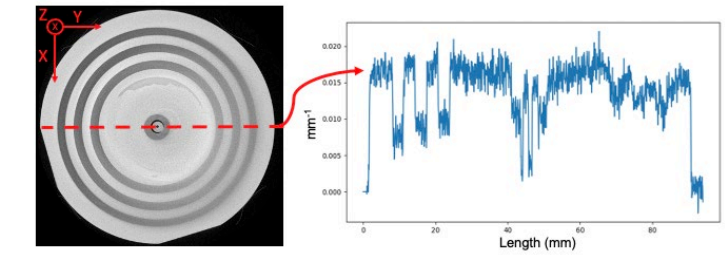

(a) CT Reconstruction

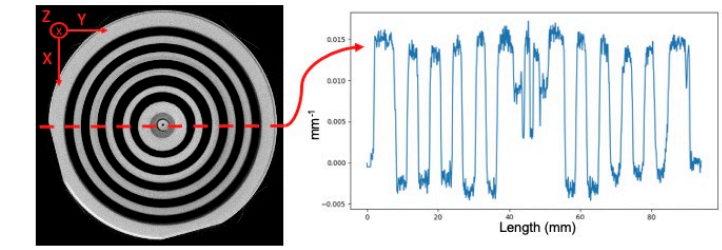

(b) Fused Result

Fig. 13. Central horizontal slice with lineout of x-ray CT reconstruction (a), central horizontal slice with lineout of fused result (b). Contrast for each ring is more consistent after fusion and smallest two inner grooves that are too subtle for x-ray CT to discern are now visible.

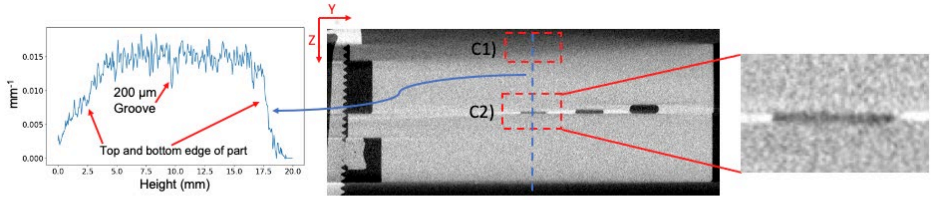

(a) CT Reconstruction

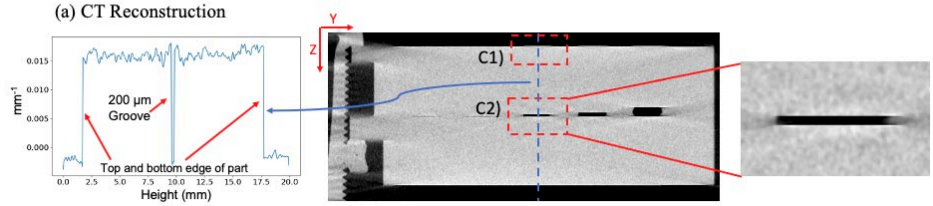

(b) Fused Result

Fig. 14. Central vertical slice of x-ray CT reconstruction (a) and fused result (b). Top and bottom edge of the sample are clearly defined after fusion. C1/C2 are the regions used for CNR metric calculations. C2 (region centered on 200 µm groove) is shown in a greater detail blowout on the right in both a) and b) for qualitative inspection.

Table 3. CNR metrics (Eq. 7) for regions C1, C2, in x-ray CT alone and in fused result. Higher values indicate improved contrast between material and background.

Region used for CNR	CNR in x-ray CT alone	CNR of fused result
C1	2.17	28.2
C2	1.37	5.12

Table 4. Estimates of groove and sample height using FWHM in x-ray CT, ultrasound, and fused result. Estimates were calculated from lineouts drawn from cross-sectional images in the volumes.

Section of sample	Specifications (mm)	Ultrasound (mm)	X-ray CT (mm)	Fused result (mm)
200µm Groove	0.20	0.28	0.43	0.25
Top-to-bottom Edge	16	15.92	14.18	15.95

6. Conclusions

Here we successfully demonstrated that under controlled conditions, ultrasound data can be effectively fused with cone-beam x-ray CT data to reveal greater interior detail using the CT-F technique presented here. Our method integrates ultrasound edge data with x-ray CT along axial edges that results in increased image quality not possible with either measurement technique alone. In contrast to previous work, our approach uses 3D Fourier filtering on the reconstruction directly to provide rapid fusion when compared to iterative methods. While other methods work for 2D slices or mainly provide improvement along external boundaries, our approach provides enhanced information along both outside edges and internal voids. Potential limitations to consider are that access to both sides of the sample is necessary during ultrasound measurement to acquire sufficient edge information. Further investigation is required to

determine how well this method can be applied to more complex shapes. Although the application here was evaluated on a homogenous sample due to ultrasound limitations, additional study is needed to understand under which conditions the fusion method can be applied with other modalities such as chromatic confocal microscopy.

Acknowledgements

This work was supported by the LLNL Laboratory Directed Research and Development Program under LLNL-LDRD 20-SI-001. Work was performed under the auspices of the U.S. Department of Energy by Lawrence Livermore National Laboratory under Contract DE-AC52-07NA27344, document number LLNL-JRNL-825755. The authors would like to acknowledge the efforts of Joe Nicolino in preparing the specimens and acquiring the data described in this paper. They would like to thank Drs. Doug Rotman, Chris Spadaccini, Ibo Matthews, and Eric Duoss for their helpful conversations and support.

References

[1] Wein, Wolfgang, Barbara Röper, and Nassir Navab. "Automatic registration and fusion of ultrasound with CT for radiotherapy." *International Conference on Medical Image Computing and Computer-Assisted Intervention*. Springer, Berlin, Heidelberg, 2005.

[2] Ewertsen, Caroline, et al. "Real-time image fusion involving diagnostic ultrasound." *American Journal of Roentgenology* 200.3 (2013): W249-W255.

[3] Schrapp, Michael, Matthias Goldammer, Karsten Schörner, and Jürgen Stephan. "Improvement of image quality in computed tomography via data fusion." In *Proceedings of the 5th International Conference on Industrial Computed Tomography (iCT)*, pp. 283-289. 2014.

[4] Liu, Yu, et al. "Cooperative data fusion of transmission and surface scan for improving limited-angle computed tomography reconstruction." *Ndt & E International* 83 (2016): 24-31.

[5] Grangeat, Pierre. *Analyse d'un système d'imagerie 3D par reconstruction à partir de radiographies X en géométrie conique*. Ph.D. Diss., l'Ecole Nationale Superieure de Telecommunications (ENST), Grenoble, France, 1987.

[6] Finch, David V. "Cone beam reconstruction with sources on a curve." *SIAM Journal on Applied Mathematics* 45.4 (1985): 665-673.

[7] Tuy, Heang K. "An inversion formula for cone-beam reconstruction." *SIAM Journal on Applied Mathematics* 43.3 (1983): 546-552.

[8] Lee, Seung Wook, Gyuseong Cho, and Ge Wang. "Artifacts associated with implementation of the Grangeat formula." *Medical physics* 29.12 (2002): 2871-2880.

[9] Bartolac, Steven, et al. "A local shift-variant Fourier model and experimental validation of circular cone-beam computed tomography artifacts." *Medical physics* 36.2 (2009): 500-512.

[10] Azevedo, S., Rizo, P. and Grangeat, P., 1995. *Region-of-interest cone-beam computed tomography* (No. UCRL-ID-121668). Lawrence Livermore National Lab., CA (United States).

[11] Pack, Jed Douglas, et al. "Method and system for reconstruction of tomographic images." U.S. Patent No. 8,805,037. 12 Aug. 2014.

[12] Sidky, Emil Y., and Xiaochuan Pan. "Image reconstruction in circular cone-beam computed tomography by constrained, total-variation minimization." *Physics in Medicine & Biology* 53.17 (2008): 4777.

[13] Chen, Guang-Hong, Jie Tang, and Shuai Leng. "Prior image constrained compressed sensing (PICCS): a method to accurately reconstruct dynamic CT images from highly undersampled projection data sets." *Medical physics* 35.2 (2008): 660-663.

[14] Krautkrämer, Josef, and Herbert Krautkrämer. *Ultrasonic testing of materials*. Springer Science & Business Media, 2013.

[15] Hellier, Charles J. *Handbook of nondestructive evaluation*. McGraw-Hill Education, 2013.

[16] Maintz, JB Antoine, and Max A. Viergever. "A survey of medical image registration." *Medical image analysis* 2.1 (1998): 1-36.

[17] Viergever, Max A., et al. "A survey of medical image registration–under review." (2016): 140-144.

[18] Champley, Kyle. "Livermore tomography tools (LTT) technical manual." *LLNL Software Manual, LLNL-SM-687016, Dec* (2016).

[19] Feldkamp, Lee A., Lloyd C. Davis, and James W. Kress. "Practical cone-beam algorithm." *Josa a* 1.6 (1984): 612-619.

[20] MATLAB. (2020). version 9.8.0 (R2020a). Natick, Massachusetts: The MathWorks Inc.